*Ultrasound in Med. & Biol.* Vol. 17, No. 3, pp. 265–281, 1991
Printed in the U.S.A.

0301–5629/91 $3.00 + .00


●*Original Contribution*

# PULSE-ECHO IMAGING USING A NONDIFFRACTING BEAM TRANSDUCER

J.-Y. Lu and J. F. Greenleaf
Biodynamics Research Unit, Department of Physiology and Biophysics, Mayo Clinic, Rochester, MN 55905, USA

(*Received* 13 *June* 1990; *in final form* 25 *October* 1990)

**Abstract—Conventional ultrasonic transducers generate beams that diffract as they travel. This phenomenon causes images produced in B-mode to be degraded in the far-field of the transducers. Focused transducers are used to improve image quality. Unfortunately, focused transducers have short depth of field. Although multiple pulse transmissions focused at several depths are used to increase the effective depth of field, imaging frame rate is reduced dramatically leading to blurred images of moving objects such as the heart. We present a family of transducers that produce nondiffracting beams of large depth of field. Therefore, uniformly high resolution throughout the imaging area can be obtained without sacrificing the imaging frame rate. In addition, the nondiffracting property of these beams makes the correction for beam diffraction negligible in tissue characterization. This paper reports the results of computer simulations as well as *in vitro* and *in vivo* pulse-echo imaging experiments with a nondiffracting transducer. Images are compared to those obtained by conventional focused Gaussian shaded beam transducers and a commercial ACUSON 128 B-scanner. The new transducer has much longer depth of field with higher sidelobes than conventional transducers of the same aperture. Sidelobes can be reduced using the new transducer to transmit and the dynamically focused transducer to receive.**

***Key Words:*** **Nondiffracting beam, Nondiffracting transducer, Ultrasonic transducer, Bessel beam, Gaussian beam, Pulse-echo imaging, Tissue samples, Tissue equivalent phantom, Calibration of receiver, Dynamic focusing.**

## INTRODUCTION

Gaussian-shaded focused ultrasonic beams produce sharp B-scan images of biological soft tissues in their focal region. Images out of that region are blurred because the depth of field of the focused beam is short. To solve this problem, dynamic focusing and multiple transmission focal depths are used. This requires complicated electronics and leads to the problem of low frame rate which results in blurred images of moving objects such as the heart. If a beam with large depth of field could be produced, multiple transmission focal depths would not be required to obtain uniform focus throughout the image.

Recently, Durnin (1987) discovered a theoretical nondiffracting solution to the scalar wave equation, which described a beam that travels to infinity without spreading, given an infinite aperture. Even for practical finite apertures the beam had very large depth of field. Hsu et al. (1989) have applied Durnin's theory to ultrasonic transducer design and have made a PZT nondiffracting transducer using a nonuniform poling technique. Ziolkowski et al. (1989) have simulated a nondiffracting acoustic pulse wave using superposition but did not use the entire array simultaneously. These studies of nondiffracting acoustic waves were very limited and none of them applied to medical imaging. We developed a 10 element $J_o$ Bessel ultrasonic nondiffracting annular array transducer using a PZT ceramic/polymer composite and have reported its nondiffracting characteristics and medical imaging feasibility for both continuous-wave and pulsed-wave conditions. A beam of depth of field over 200 mm with a −6 dB center lobe beam diameter of 2.53 mm was produced (Lu and Greenleaf 1990).

This paper reports the results of *in vitro* and *in vivo* pulse-echo imaging experiments using the $J_o$ Bessel nondiffracting transducer and compares them to images obtained with a conventional focused Gauss-

Address correspondence to: Dr. Jian-yu Lu, Biodynamics Research Unit, Department of Physiology and Biophysics, Mayo Clinic, 200 First Street SW, Rochester, MN 55905, USA

ian beam transducer (focal length = 120 mm) and a commercial ACUSON 128 B-scanner. The transducer used for imaging has 10 annular elements and its radius and center frequency are 25 mm and 2.5 MHz, respectively. In the next section, the concepts of the nondiffracting beam and the conventional Gaussian beam are briefly reviewed. In the third section, the experimental system is described and in the fourth section, simulation, *in vitro* and *in vivo,* experimental results are given. The last section covers the discussion and conclusion.

## NONDIFFRACTING BEAM AND CONVENTIONAL GAUSSIAN BEAM

A nondiffracting solution of the source-free scalar wave equation was discovered by Durnin (1987):

$$U(\vec{r}, t) = e^{j(\beta z - \omega t)}\left[\int_o^{2\pi} A(\phi)e^{-j\alpha(x\cos\phi + y\sin\phi)}d\phi\right] \quad (1)$$

where

$$\begin{cases} \alpha^2 + \beta^2 = k^2, \left(k = \dfrac{\omega}{c}\right), \\ o < \alpha \leq k. \end{cases} \quad (2)$$

$A(\phi)$ is an arbitrary complex function of $\phi$, $\phi$ is the integration variable, $U(\vec{r}, t)$ is sound pressure, $\vec{r} = (x, y, z)$ represents the spatial observing point, $t$ is time, $\omega$ is angular frequency, and $c$ is the sound speed. $\alpha$ is a constant which determines the width of the center lobe of the beam. $\beta$ is related to $\alpha$ by eqn (2) and is frequency dependent.

If $A(\phi)$ is independent of $\phi$, one obtains the simplest axial symmetric nondiffracting solution,

$$U(\vec{r}, t) = J_o(\alpha\rho)e^{j(\beta z - \omega t)} \quad (3)$$

where $J_o$ is the zeroth order Bessel function of the first kind, $\rho = \sqrt{x^2 + y^2}$ is the distance away from the center axis of the transducer, and $\alpha$ is a scaling factor of the $J_o$ Bessel function. From eqn (3), it is seen that the beam pattern of the $J_o$ Bessel nondiffracting solution is independent of distance, $z$. This indicates that the $J_o$ Bessel beam will travel to infinity without changing shape (diffracting).

If the $J_o$ Bessel beam is truncated symmetrically by an aperture of radius $a$, the maximum nondiffracting distance, defined by Durnin (1987) is given by

$$Bz_{\max} = a\sqrt{(k/\alpha)^2 - 1}. \quad (4)$$

For comparison, a conventional Gaussian beam has the following profile (Hsu et al. 1990):

$$G(\rho, z) = A[\sigma(o)/\sigma(z)]e^{-\rho^2/\sigma^2(z)} \quad (5)$$

where

$$\sigma(z) = [\lambda/(\pi\sigma(o))]\sqrt{z^2 + \pi^2\sigma^4(o)/\lambda^2}. \quad (6)$$

$A$ is a constant, $\lambda$ is the wavelength of the wave in surrounding medium, $\sigma(o)$ is the half width of the beam (defined as the distance away from the center of the beam at which the amplitude of the beam drops to $1/e$ of its maximum) at the surface of the transducer, and $\rho$ is the distance away from the center of the beam. Unlike the nondiffracting beam, the Gaussian beam will spread wider and wider as it travels farther and farther away from the transducer. If an acoustical lens is attached to the transducer surface, the Gaussian beam will be focused at a certain distance. Previously reported computer simulations and experiments for the fields of the focused Gaussian beam (Lu and Greenleaf 1990) demonstrated that when the focused Gaussian beam is applied for imaging, only the region around its focus will have high lateral resolution.

## EXPERIMENTAL SYSTEM

*Pulse-echo imaging system*

A schematic of the pulse-echo imaging system employed for experiments is shown in Fig. 1. A DATA 2045 Polynomial Waveform Synthesizer† was used to generate a short electrical pulse of about one and a half cycles. The 10 pulse amplitudes for each of the 10 rings were shaded according to $J_o$ Bessel or Gaussian functions by the Transmitting and Receiving Circuit driving the 10 element annular array transducer. The 10 received echoes were amplified and shaded according to $J_o$ Bessel or Gaussian functions by a set of receiving amplifiers. The signals from the transducer elements were summed, filtered by a Band-pass Filter (lower and higher cutoff frequencies are 1 MHz and 4 MHz, respectively), and sent to the Amplifier (the group of amplifiers were capable of linear amplification, *rf* log compression, and time-variable-gain compensation). The final *rf* signal was detected, low-pass filtered (cutoff frequency is 1 MHz), digitized by an 8-bit A/D converter (the sampling rate was programmable through the Controlling Computer), and transferred to a SUN workstation for image construction.

The transducer was moved by the stepping mo-

† Data Precision of Analogic Corporation, Peabody, MA, USA.

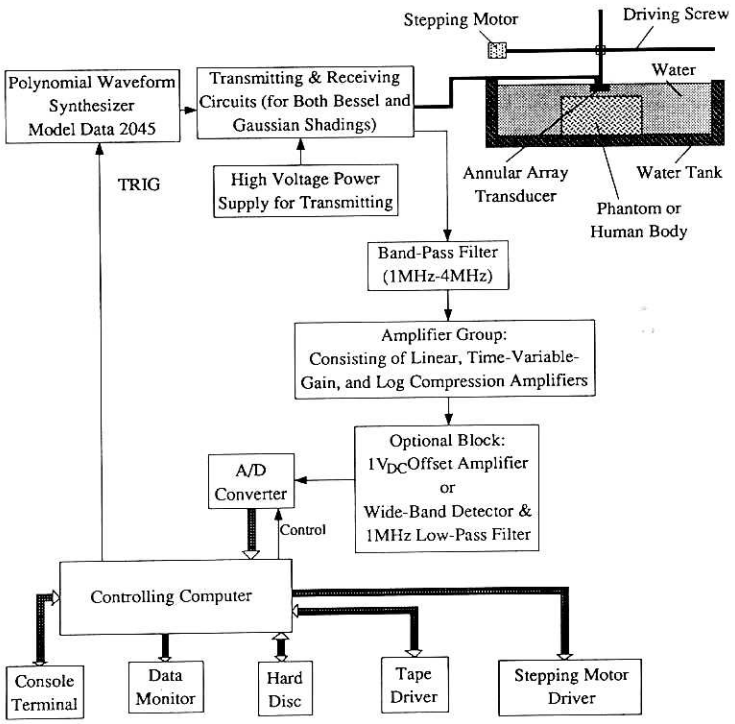


Fig. 1. Block diagram of the experimental system for pulse-echo imaging. The same annular array (Fig. 2) can be used for producing Bessel or Gaussian beams.

tor which was controlled by the computer. Once the transducer reached a desired position, a signal from the computer triggered the DATA 2045 Polynomial Waveform Synthesizer to generate a short electrical pulse to excite the transducer elements. After a preset delay, the A/D converter was triggered to digitize echo signals to form an A-line. Scanning the transducer and repeating the process produced the B-scan images.

*$J_o$Bessel nondiffraction transducer and its Bessel and Gaussian shading*

The structure of the $J_o$ Bessel nondiffracting transducer is shown in Fig. 2. It is a 10 element annular array transducer with annular element edges determined by positions of zeroes of the $J_o(\alpha\rho)$ Bessel function with a scaling parameter $\alpha = 1202.45\ \text{m}^{-1}$. [The bigger the parameter $\alpha$ is, the smaller the size of the main beam lobe, and the shorter the maximum nondiffracting distance (see eqn 4).] Spacing between the edges of any two successive elements is less than 0.2 mm. The diameter of the transducer is 50 mm. The transducer is made of PZT ceramic/polymer 1-3 composite. It is broadband with its −6 dB bandwidth around 50% of its center frequency (2.5 MHz). The transducer is backed with low impedance and matched to water with a front matching layer. The radius of the center element of the transducer is 2 mm. The nondiffracting distance $Bz_{\max}$ calculated from eqn (4) is 216 mm.

From Fig. 2 it is seen that the $J_o$ Bessel nondiffracting transducer is really an annular array transducer with a special arrangement of the elements. Therefore, it can be shaded to produce either Bessel or Gaussian beams. The exact plots of $J_o$ Bessel function $J_o(\alpha\rho)$ and Gaussian function $(e^{-\rho 2/\sigma 2})$ (where $\alpha = 1202.45\ \text{m}^{-1}$ and $\sigma = 15$ mm) in eqns (3) and (5) are shown by dotted lines of Figs. 3(a) and 3(b), respectively. Because the voltages (both imposed an induced) across each element of the transducer are uniform, stepwise approximations of the $J_o$ Bessel and Gaussian functions result [see the solid lines in Figs. 3(a) and 3(b)].

Figures 4(a) and 4(b) are computer simulations of pulse-echo responses of a point scatterer with $J_o$ Bessel and focused Gaussian shadings, respectively. Dashed and solid lines represent the results with exact shadings and their stepwise approximations (see Fig. 3), respectively. Panels (1), (2), and (3) in both Figs. 4(a) and 4(b) correspond to the lateral responses (perpendicular to the transducer axis and through the pulse maxima) with the point scatterer placed at distances $z = 50$ mm, 120 mm, and 216 mm away from the transducer on the center axis, respectively. Panel (4) represents the maximum of the pulse-echo response of the point scatterer along the center axis of

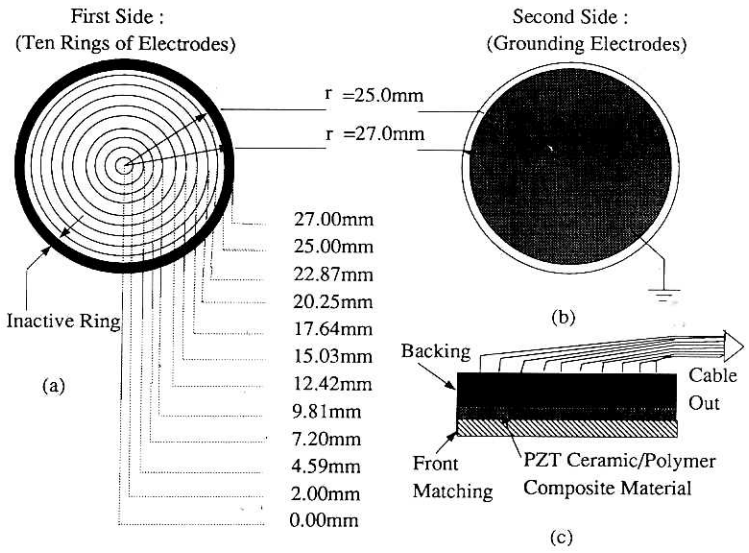


Center Frequency: 2.5MHz
Space Between the Rings:<0.2mm
Bandwidth: > 50% of the Center Frequency

Fig. 2. $J_o$ Bessel nondiffracting transducer which is an annular array transducer with electrode cutting on zeros of $J_o$ Bessel function.

the transducer. Lateral distances are normalized to pulse center wavelength which is 0.6 mm, and axial distances are normalized to $J_o$ Bessel beam center lobe width [4 mm between the first zeros of $J_o(\alpha\rho)$, in Fig. 4(a)], and the diameter of the transducer [50 mm, in Fig. 4(b)]. In the simulation, the pulse-echo impulse response of the transducer was assumed to be the convolution of the following function with itself:

$$f(t) = e^{-t^2/t_o^2} \sin 2\pi f_o t \qquad (7)$$

where $t_o$ = 0.4 $\mu$s and $f_o$ = 2.5 MHz, and the transducer was assumed to be excited by an electrical $\delta$-pulse.

*Calibration of the transducer*

Calibration of the electrical drive for each ring in transmitting was required to ensure accurate Bessel shaped pressure fields. First, we computed the sound pressure at ($\rho$, $z$) = (0 mm, 205 mm) that should be produced by driving each of the annuli individually with the Gaussian or Bessel value of voltage appropriate to its radius. Then, by placing a hydrophone (diameter = 0.5 mm) at the same distance in a water tank, each element of the transducer was excited individually and the excitation voltages were adjusted to produce the respective calculated pressure values for either $J_o$ Bessel or Gaussian shading (Lu and Greenleaf 1990).

In receiving, a coherent Bessel or Gaussian weighted summation of electrical charges induced by acoustical pressures on the annular elements was required. To ensure a $J_o$ Bessel or Gaussian relationship between the pressure and the output voltage, a point source was placed at certain distance, say, $z$ = 410 mm on the center axis of the transducer, and the induced charges on the elements were computed. These computed charges were then weighted according to the stepwise approximations of the $J_o$ Bessel or Gaussian functions shown in Fig. 3.

In our experiment, a PZT ceramic/polymer 1-3 composite transducer with a diameter of 4 mm was used as a point source and placed at the distance $z$ = 410 mm. Because there is a relationship between the induced charge and the measured voltage for each element

$$v_i = \frac{q_i}{C_i} \quad (i = 1, 2, \cdots, 10), \qquad (8)$$

where $v_i$, $q_i$, and $C_i$ are voltage, charge, and capacitance of the $i$th element, respectively, the voltage $v_i$ can be used to represent the charge $q_i$. Summation over the weighted charges of the elements gives

$$S = \sum_{i=1}^{10} w_i q_i \qquad (9)$$

which represents the received signal of stepwise $J_o$ Bessel or Gaussian shading (where $w_i$ are the approximate $J_o$ Bessel or Gaussian weights obtained from Fig. 3). The weighted charge, $w_i q_i$, that should be produced by each element due to the point source excitation was adjusted with attenuators to have the values determined by Table 1 (weighted charges of outer elements were normalized relative to the central element).

*Broadband application of the nondiffracting transducer*

The original suggestion of the nondiffracting beam by Durnin was in harmonic (CW) form (Durnin 1987). Ultrasonic imaging requires broadband application of the nondiffracting beam.

Equation (3) represents the nondiffracting beam with infinite aperture. From this equation, a broadband pulse can be synthesized:

$$U(\vec{r}, t) = \frac{1}{2\pi}\int_{-\infty}^{\infty} [J_o(\alpha\rho)e^{+j\beta z}]\bar{e}^{j\omega t}d\omega \quad (10)$$

or

$$U(\vec{r}, t) = J_o(\alpha\rho)\left\{\frac{1}{2\pi}\int_{-\infty}^{\infty} \bar{e}^{j(\omega t-\beta z)}d\omega\right\}. \quad (11)$$

From eqn. (11), it is seen that the pulse is nondiffracting in the sense that its lateral shape ($J_o$ Bessel distribution) is independent of time, $t$, and axial distance, $z$. The axial shape of the pulse is determined by the brace term of eqn (11) which is a function of time, $t$, and the axial distance, $z$. The magnitude of $|e^{j\beta z}| \equiv 1$ as long as $|k| > \alpha$ [if $\alpha = 1202.45\ \text{m}^{-1}$, $f$ must be greater than 0.287 MHz, see eqn (2)]. This indicates that the infinite aperture nondiffracting beam system is a high-pass spatial filtering system with a low, distance-independent cutoff frequency and is capable of broadband applications.

Figure 5(1) to (4) are simulated magnitudes of frequency spectra of pulse-echo responses for a finite aperture transducer system shaded by a $J_o$ Bessel function, $J_o(\alpha\rho)$, when a scatterer is placed on the

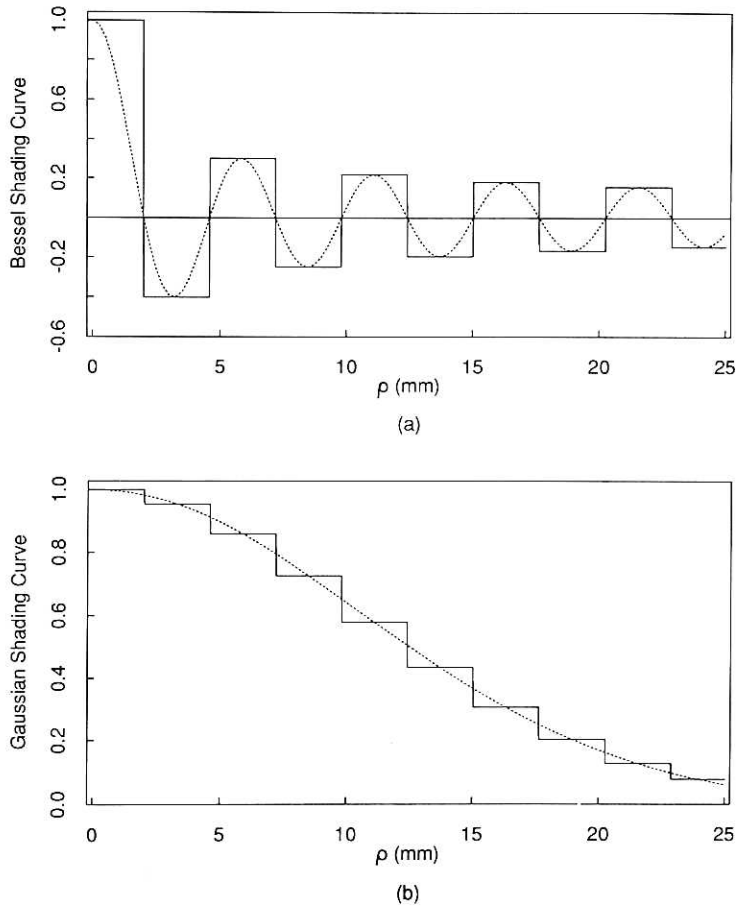


Fig. 3. Shadings used for the 10 element annular array transducer are symmetric about $\rho = 0$. (a) $J_o$ Bessel and (b) Gaussian shading curves (dotted lines) and their stepwise approximations (solid lines).

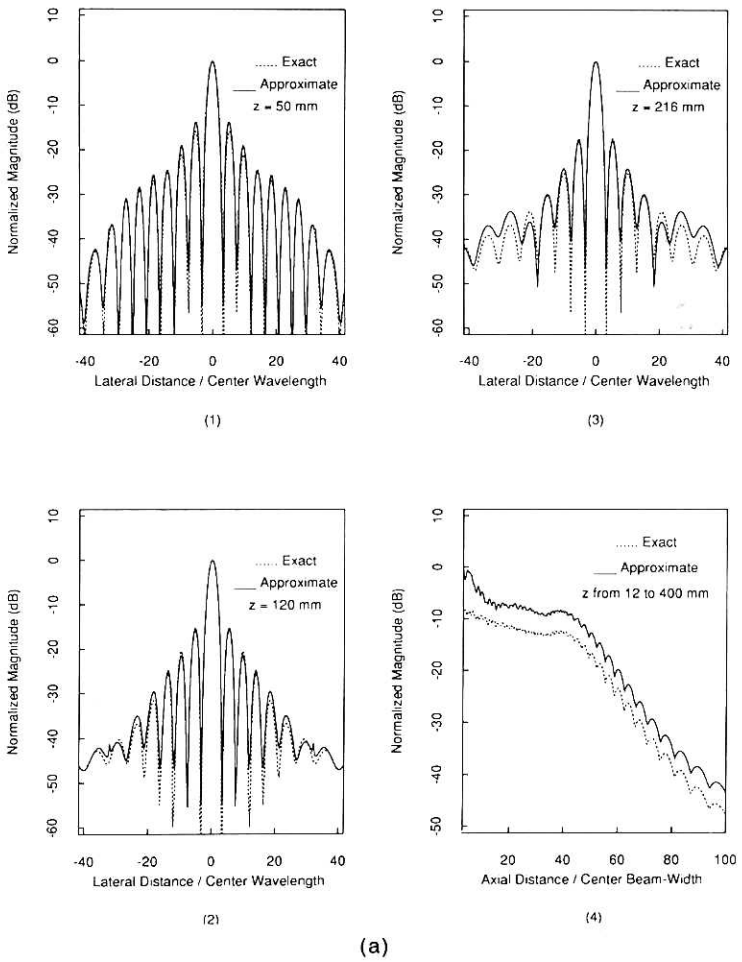


Fig. 4. Comparison of pulse-echo response of the transducer from a point scatterer with exact shading (dashed lines) and stepwise shading (solid lines). (a) and (b) are the responses corresponding to $J_o$ Bessel shading and focused Gaussian shading, respectively. (1), (2), and (3) are the lateral responses (through the peaks of the responses) at distances $z$ = 50 mm, 120 mm (focal length of Gaussian beam), and 216 mm, respectively. (4) shows the maxima of the responses when the point scatterer is moved from 12 mm to 400 mm away from transducer on the center axial axis. Center wavelength is 0.6 mm, beam width of Bessel beam (between two first zeros) is 4 mm and diameter of transducer is 50 mm.

central axis of the transducer at distances $z$ = 50 mm, 100 mm, 150 mm, and 216 mm away from the transducer, respectively. In simulation, the diameter of the transducer, $D$, and the scaling factor of the $J_o$ Bessel function, $\alpha$, were assumed to be 50 mm and 1202.45 $m^{-1}$, respectively. The transmitting and receiving transfer functions of the transducer material were not included. The vertical dashed lines in Fig. 5 correspond to the −6 dB pulse-echo bandwidth of our transducer. From Fig. 5, it is seen that a finite aperture nondiffracting transducer is a spatial high-pass filtering system, and its cutoff frequency increases with distance. Therefore, within a certain range, a nondiffracting transducer can be used to produce broadband pulses. This is verified by experiment in the following section.

## SIMULATION AND EXPERIMENTAL RESULTS

*Pulse-echo imaging of bead phantom*

Figure 6(a) shows the arrangement of glass beads in our resolution phantom (bead phantom). The relative positions of the beads are also described in the figure. Figure 6(b) is a photograph of the phantom which was composed of small glass balls with a diameter of 0.83 mm. Each glass ball was connected to one end of a glass rod of diameter 0.16 mm and length of 24 mm. The other end of the glass rod was glued to a flattened Saran wrap film of thickness of 0.009 mm with LOCTITE 494 superbonder. The rods were tilted by 60° with respect to the acoustic wave incident direction to reduce reflections from the rods.

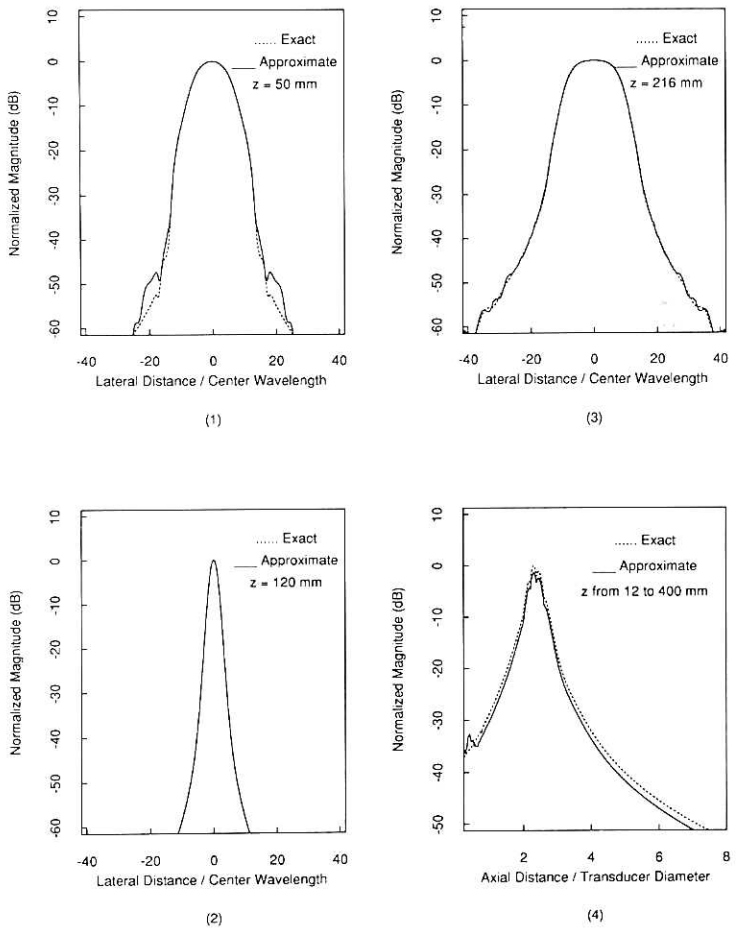


(b)

Fig. 4. *Continued.*

Figures 7(a) and 7(b) are experimental results with $J_o$ Bessel and Gaussian shaded transducers, respectively. The electrical excitation pulse of the transducer was of the form of eqn (7) and the transducer used was that described in Fig. 2. In the case of Gaussian shading, focus was achieved by attaching a plexiglass acoustic lens with a focal length of 120 mm to the front of the transducer. The four panels in Fig. 7(a) were obtained when the phantom was placed at distances $z$ = 50 mm, 100 mm, 150 mm, and 216 mm, respectively. The size of each panel is 15.36 mm (axial) × 50 mm (lateral) with pixel size of 0.06 mm × 0.25 mm. The four panels in Fig. 7(b) were obtained at distances $z$ = 50 mm, 120 mm, 150 mm, and 216 mm, respectively.

To form the images in Figs. 7(a) and 7(b), the signals were first amplified by using linear amplifiers in Fig. 1 and offset by 1 $V_{DC}$ (the offset was required by the input range of the A/D converter). The linear $rf$ signals were then digitized at a sampling frequency of 40 MHz. A SUN workstation was used for calculation of the envelopes of the signals and for image constructions.

Figure 8 shows lateral and axial plots of the experimental pulse-echo responses (solid lines) of the bead phantom through the maxima of the left-most beads

Table 1. Weighted charges from elements of transducer before summation in receiving ($z$ = 410 mm).

| Element # | 1 | 2 | 3 | 4 | 5 | 6 | 7 | 8 | 9 | 10 |
|---|---|---|---|---|---|---|---|---|---|---|
| Bessel beam | 1.00 | 1.76 | 2.35 | 2.80 | 3.18 | 3.50 | 3.77 | 4.00 | 4.19 | 3.75 |
| Gaussian beam | 1.00 | 4.15 | 6.70 | 8.14 | 8.42 | 7.72 | 6.40 | 4.86 | 3.40 | 2.00 |

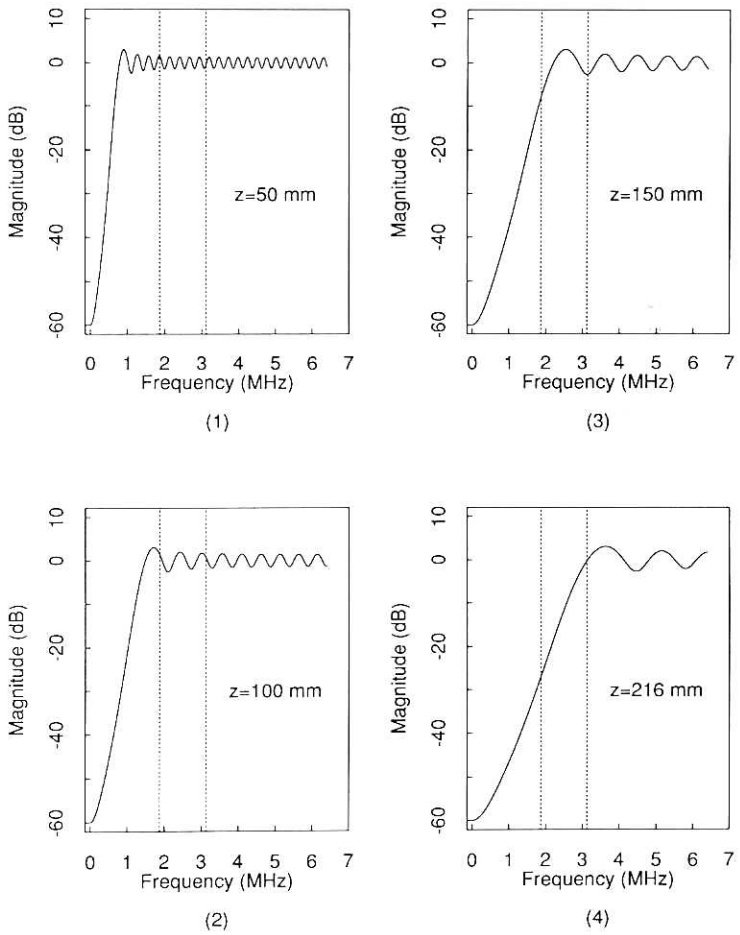


Fig. 5. Spatial filtering properties of nondiffracting pulse-echo system. (1), (2), (3), and (4) are the magnitude of the frequency responses (solid lines) of a point scatterer placed at distances $z$ = 50 mm, 100 mm, 150 mm, and 216 mm, respectively. Dashed lines represent the −6 dB pulse-echo bandwidth of the transducer.

in Fig. 7. Figures 8(a) and 8(b) represent the results from $J_o$ Bessel shaded and focused Gaussian shaded transducers, respectively. The left-hand side panels in Figs. 8(a) and 8(b) are lateral responses of the left-most beads and the right-hand side panels axial responses through three beads. From top to bottom, the bead phantom was placed at the distances $z$ = 50 mm, 100 mm, and 216 mm (for Bessel shading) and 50 mm, 120 mm, and 216 mm (for focused Gaussian shading) away from the transducer. The center wavelength of the pulse was 0.6 mm.

The dashed lines in Fig. 8 are simulation results for the experimental conditions which produced the measured solid line profiles. The results of Fig. 8 indicate that the new transducer configuration produces nondiffracting pulses over a range from 50 mm to 200 mm. This is in contrast to the strongly diffracting focused Gaussian beam which is defocused at 50 mm and 200 mm. The lateral point resolution of the Bessel beam is better than that of the focused Gaussian beam, but the sidelobes are worse. We will address these issues separately.

*Pulse-echo imaging of RMI413A tissue equivalent phantom*

We tested the point resolution of the $J_o$ Bessel nondiffracting transducer by comparing its pulse-echo images with those of a fixed focus transducer and with the ACUSON scanner. Figure 9 is a cross-section of a commercial RMI413A‡ tissue equivalent phantom. The phantom was composed of nylon wires of diameter 0.3 mm and thin plastic tubes filled with echoless fluid. The dimension of the pattern is shown in Fig. 9. The enlarged resolution pattern is shown at the bottom of the figure. The spaces between wires were full of tissue mimicking scattering material with

‡ Radiation Measurements, Inc., Middleton, WI 53562, USA.

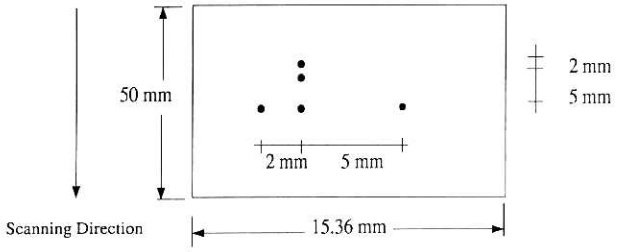


(a)

(b)

Fig. 6. Bead phantom for both computer simulations and experiments. The beads were made of glass balls of 0.83 mm in diameter. (a) Geometry and (b) photograph of the bead phantom.

attenuation and sound speed of 0.7 dB/cm/MHz and 1540 m/s, respectively.

Figures 10(a) and 10(b) are pulse-echo images of the RMI413A tissue equivalent phantom obtained by $J_o$ Bessel and Gaussian shaded annular array transducers, respectively. "<" in Fig. 10(b) indicates where the beams are focused and will be used in the following figures. A time-variable-gain amplifier, Fig. 1, was used to compensate the attenuation of the phantom and the $rf$ signals were DC offset and digitized at 40 megasamples/second. Analytic envelope signals of the $A$-lines were computed one by one to form images. The dimension of the images are 110 mm × 131 mm and the pixel size is 0.25 mm × 0.25 mm. The transducer was scanned at a level 30 mm above the top row of the wire reflectors.

Figure 10(c) shows the image of the same phantom obtained by an ACUSON 128 commercial B-scanner. The B-scanner was set to dynamic focusing mode in both transmitting and receiving. The dimen-

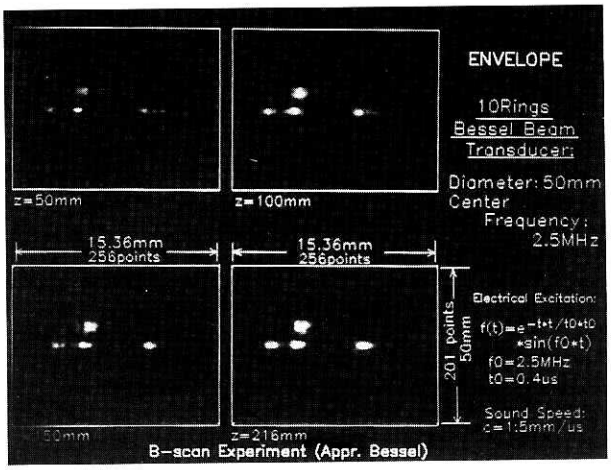


(a)

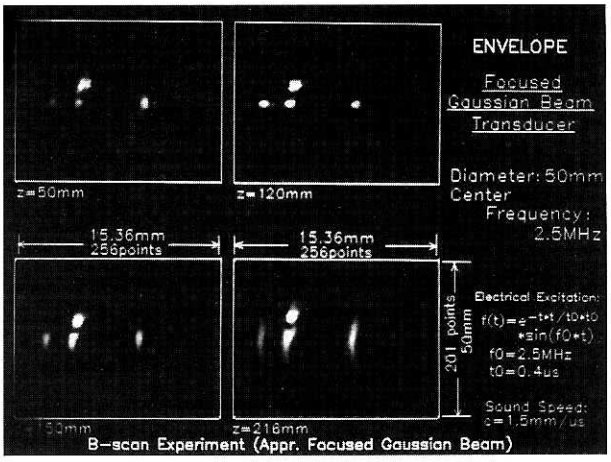


(b)

Fig. 7. Experimental results of pulse-echo imaging of bead phantom with transducer of (a) $J_o$ Bessel shading, (b) focused Gaussian shading (focal length = 120 mm) in both transmitting and receiving. The four panels in Fig. 7(a) represent the results when the phantom was placed at distances $z$ = 50 mm, 100 mm, 150 mm, and 216 mm, respectively, and the four panels in Fig. 7(b) the results when the phantom was placed at distance $z$ = 50 mm, 120 mm, 150 mm, and 216 mm, respectively. The dimension of each panel is 15.36 mm × 50 mm.

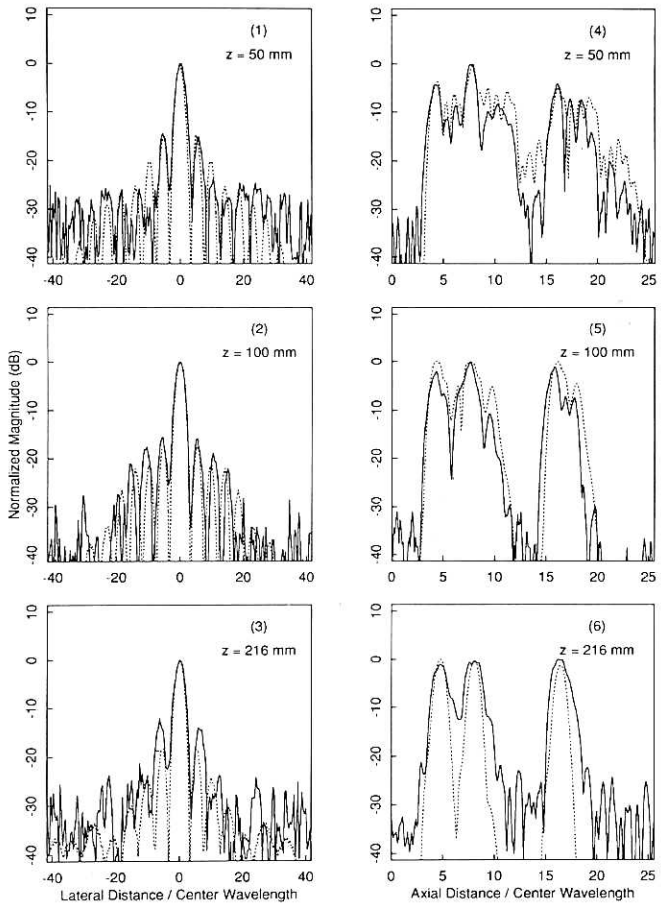


Fig. 8. Lateral [(1), (2), and (3)] and axial [(4), (5), and (6)] line plots of pulse-echo images of bead phantom. The lateral and axial line plots are perpendicular to each other and through the maxima of the pulse-echo responses of the left-most bead [see Fig. 4(a)]. (a) and (b) are obtained from $J_o$ Bessel and focused Gaussian shading (focal length = 120 mm), respectively. From top to bottom in (a), the responses were obtained with the bead phantom placed at $z$ = 50 mm, 100 mm, and 216 mm, respectively. In (b) the distances were set to $z$ = 50 mm, 120 mm, and 216 mm, respectively. Solid lines represent experimental results and dashed lines the simulations. Center wavelength of the pulse is 0.6 mm.

sions of the image were the same as those of Fig. 10(a) or Fig. 10(b). The transducer was placed 20 mm away from the top row of the wire reflectors.

*Pulse-echo imaging of sliced human liver sample*

To test the nondiffracting large depth of field imaging of the $J_o$ Bessel beam transducer, we scanned tissue samples at various distances and compared the images to those obtained with a fixed focus transducer and to an ACUSON scanner. Figure 11 shows a human tissue sample made from sliced human liver. The tissue was fixed in 10% formalin fluid for several days and then enclosed in a plexiglass box (Alasaarela and Koivukangas 1990). The top of the box was sealed by 0.125 mm thick polyester film which acted as an acoustic window. The dimensions of the sliced liver sample were 154 mm (length) × 60 mm (wide) × 100 mm (high). The liver sample was composed of six slices of livers stacked on top of one another. Guiding lines for the alignment of scanning were drawn across the acoustic window of the sample box.

Figures 12(a) and 12(b) illustrate images of the sliced human liver sample obtained with $J_o$ Bessel and focused Gaussian shaded annular array transducers, respectively. Each panel of the images represents the same area of the liver sample and the three panels in each image correspond to the position of the sample at three different distances away from the transducers, *i.e.*, $z$ = 50 mm, 100 mm, and 150 mm, respectively. The size of each panel is 82 mm × 37.5 mm and the pixel size is 0.25 × 0.25 mm.

The same procedures of signal processing in ob-

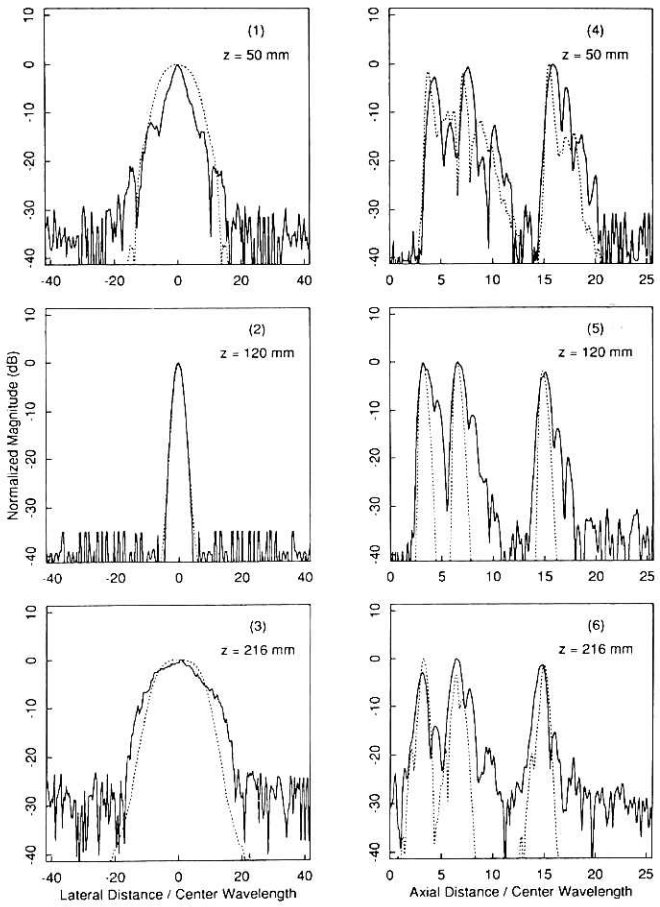


(b)

Fig. 8. *Continued.*

taining Figs. 10(a) and 10(b) were applied to produce Figs. 12(a) and 12(b), except that 20 megasamples/second sampling rate was used and the signals were log compressed before digitizing.

Figure 12(c) corresponds to Fig. 12(a) or Fig. 12(b) but was obtained by the ACUSON 128 commercial B-scanner. Dynamic focusing in both transmitting and receiving were employed.

*In vivo pulse-echo imaging of human livers*

We used a mechanical scanning arrangement to image the liver in a volunteer using the transducer of $J_o$ Bessel shading. The *in vivo* experimental system is shown in Fig. 13(a). The transducer was shaded with a $J_o$ Bessel function in both transmitting and receiving. It scanned from the midline of the belly of the volunteer toward the right side of the body and was placed below the last rib. The transducer was coupled and lubricated by ultrasound gel and the scanning distance was 82 mm. The echo signals from the body were processed the same way as to obtain the images in Fig. 12, except that the *rf* signals were detected and low-pass filtered (cutoff frequency is 1 MHz) and digitized at the sampling rate of 10 megasamples/second. In order to scan the liver, the volunteer was instructed to take and hold a deep breath until the scanning process was finished.

Figure 13(b) shows the image of the liver of the volunteer with a thin belly. The image is of the size of 82 mm (width) × 75 mm (depth) and was obtained by the $J_o$ Bessel shaded (in both transmitting and receiving) nondiffracting transducer.

## DISCUSSION AND CONCLUSION

This paper reports experimental studies of pulse-echo imaging of phantoms, tissue samples, and *in vivo* human liver using a new nondiffracting beam transducer and compares the results to those obtained by a conventional focused Gaussian beam transducer and by an ACUSON 128 commercial B-scanner. We have shown that the $J_o$ Bessel beam has a very large depth

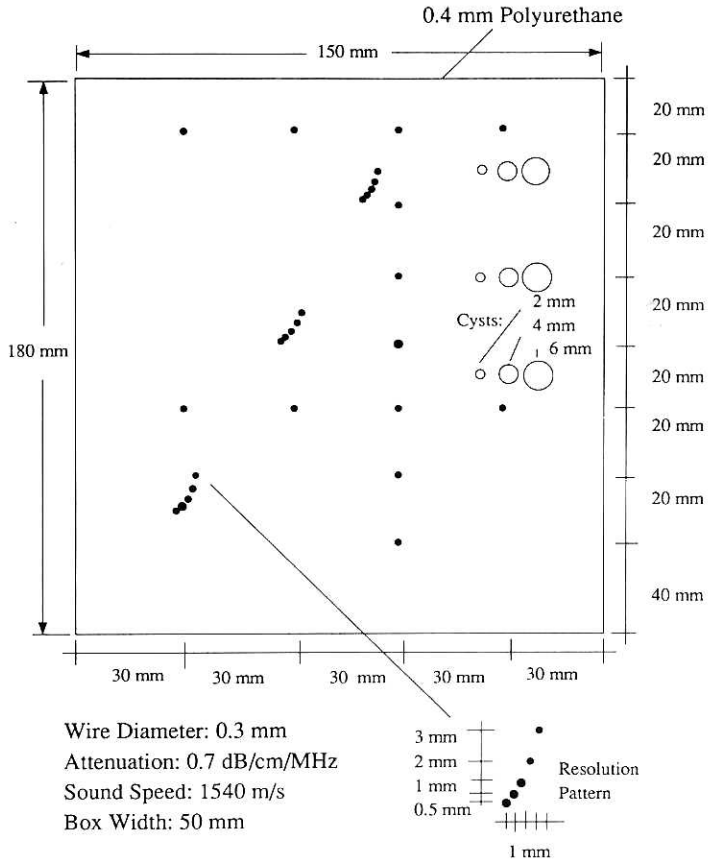


Fig. 9. Cross-section of commercial tissue equivalent phantom (RMI413A). The phantom was made of tissue mimicking material with 0.3 mm nylon wires or plastic tubes (filled with echoless fluid) embedded. The resolution patterns composed of five clustered nylon wires are described on the bottom right of the figure.

of field, and the conventional focused Gaussian beam transducer has only a small depth of field near its focus as expected. The depth of field of the conventional Gaussian beam transducer can be increased by the technique of dynamic focusing in both transmitting and receiving (as is used by ACUSON 128 commercial B-scanner), but the image frame rate will be reduced dramatically resulting in blurred images of moving objects, such as the heart.

*Resolution*

We have obtained good agreement between computer simulations and experiments in the images of the bead phantom (Figs. 7 and 8). High (lateral) resolution is obtained at all distances shown in Fig. 7(a) with the nondiffracting transducer. The focused Gaussian beam transducer generates only high-resolution images near its focus as expected. This fact can also be seen from Figs. 10 and 12. It is seen from Figs. 12(c), that the ACUSON 128 commercial B-scanner does not give clear images of objects deep in the phantoms compared to the nearer distances, although it uses dynamic focusing to increase the depth of field and generate images of uniformly high resolution. The *in vivo* experiment on the volunteer [see Fig. 13(b)] with the $J_o$ Bessel nondiffracting transducer shows a fine speckle pattern (higher resolution), which is also the case in the imaging of excised human tissue [see Fig. 12(a)]. Figure 13(b) shows that the surface of the liver and structures inside the liver are clearly resolved. The image of the RMI413A commercial tissue equivalent phantom obtained with the nondiffracting transducer also illustrates uniformly high resolution. The Bessel transducer resolves the five wire resolution patterns as four at all depths of the phantom (see Fig. 10). Using the ACUSON 128 commercial B-scanner, two resolution patterns near the probe could be resolved as five wires, while the third resolution pattern which is farther away from the probe can only be resolved as four (the probe of ACUSON 128 B-scanner is 3 MHz as compared to 2.5 MHz of the nondiffracting transducer)

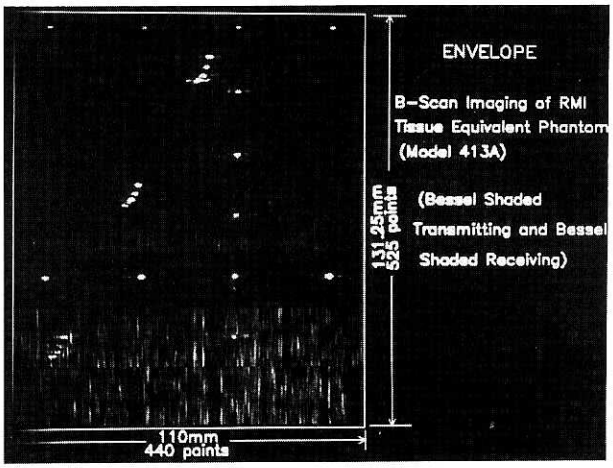


(a)

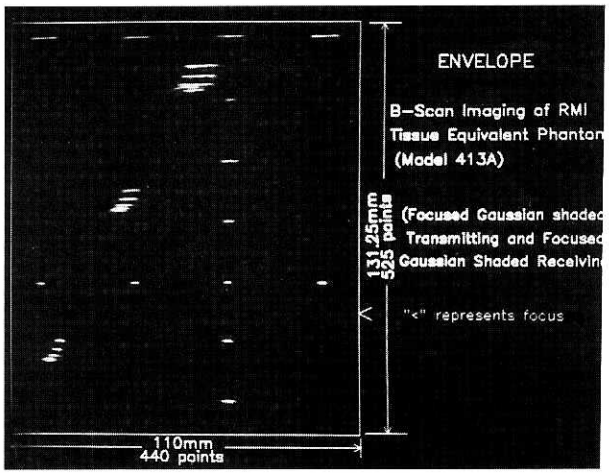


(b)

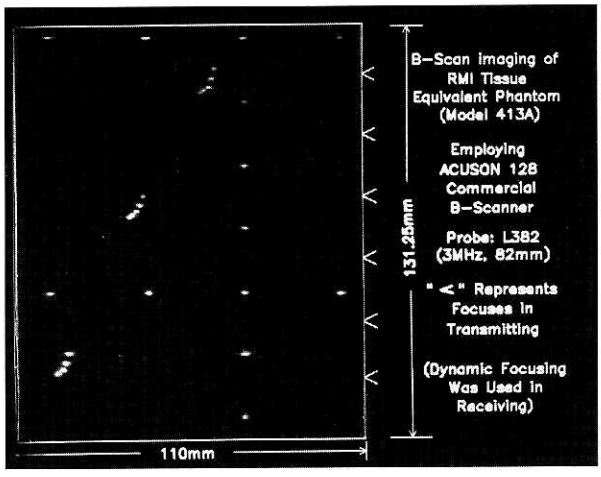


(c)

Fig. 10. B-scanning imaging of RMI413A tissue equivalent phantom. Transducer was scanned on top of the phantom. The image size is 110 mm × 131.25 mm. "<" sign represents the transmitting focuses. (a) $J_o$ Bessel shading and (b) focused Gaussian shading (focal length = 120 mm), (c) images obtained by ACUSON 128 commercial B-scanner.

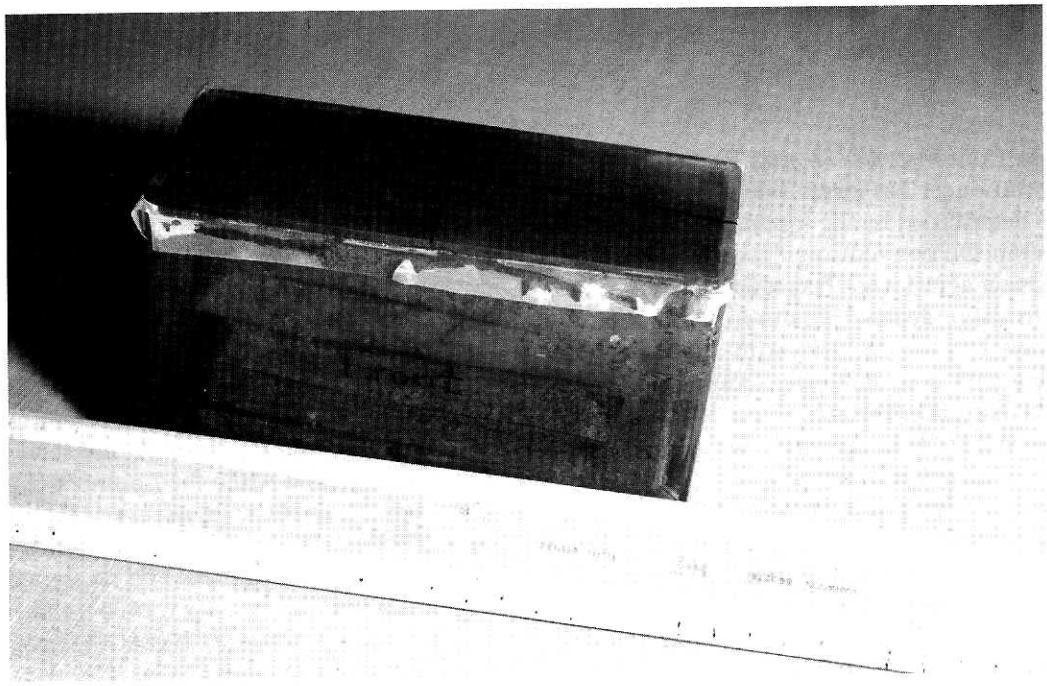

Fig. 11. Photograph of a sliced human liver sample. The liver was fixed in 10% formalin solution and sliced into six pieces and put into a plexiglass box. The top of the box was covered with polyester of thickness 0.125 mm. The dimension of the box is 154 mm × 60 mm × 100 mm.

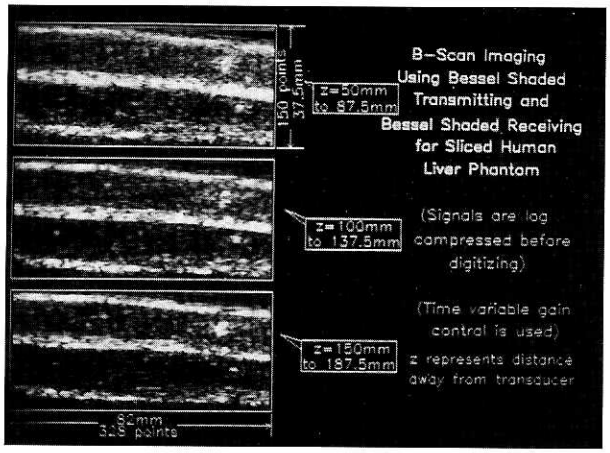


(a)

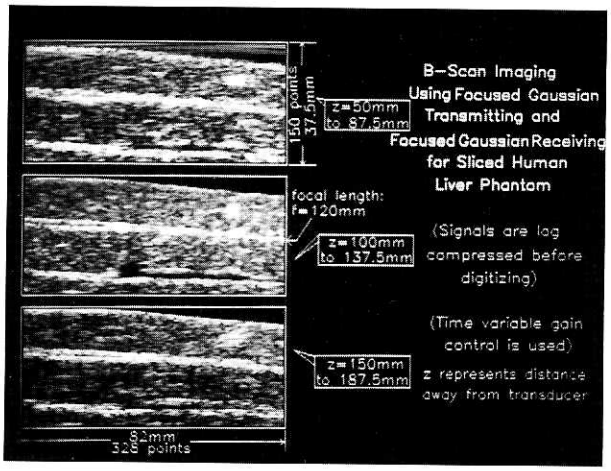


(b)

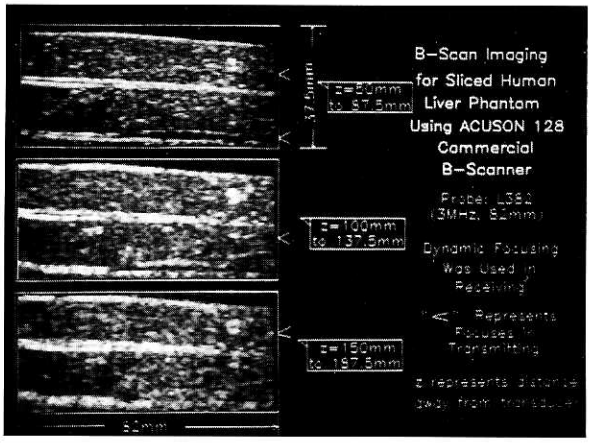


(c)

Fig. 12. B-scan imaging of sliced human liver sample. Each panel shows an image of the same region in the sample. The size of the region is 82 × 37.5 mm, and the distances of the region away from the transducer surface are indicated on the right-hand side of the panels, *i.e.*, $z$ = 50 mm, 100 mm, and 150 mm, respectively. (a) $J_o$ Bessel shading, (b) focused Gaussian shading (focal length = 120 mm), (c) images obtained by ACUSON 128 commercial B-scanner.

*Sidelobes*

It is seen from Figs. 4, 7, 8, and 10 that the nondiffracting transducer has larger sidelobes (their amplitudes are determined by the square of the $J_o$ Bessel function) than the conventional focused Gaussian beam transducer at its focus. This reduces the contrast of images to some degree. However, this problem might be solved by transmitting with a Bessel beam and receiving with a dynamically focused Gaussian (or non-Gaussian) beam which would not reduce the imaging frame rate. It is generally believed that for imaging of moving objects such as heart, the importance of sidelobe effects would be diminished because one can keep track of the moving objects in a low-contrast image. Since the impulse response of the Bessel transducer is constant over the imaging plane, deconvolution will be simple and can probably be done in real time.

To study the sidelobes of the nondiffracting beam transducer, we simulated the lateral pulse-echo responses of a point scatterer of an imaging system composed of various combinations of Bessel/Gaussian beams. Figures 14(a), 14(b), and 14(c) are the responses when $Z/D$ = 1.0, 2.4, and 4.32, where $Z$ and $D$ are the distance of the point scatterer away from the surface of transducer and the diameter of the transducer ($D$ = 50 mm), respectively. Solid lines in Figs. 14(a), 14(b), and 14(c) represent results when both transmitting and receiving are shaded with the Gaussian function while the $f$-number (focal length/diameter of transducer) is always equal to $Z/D$. This corresponds to the situation when dynamic focusing is used in both transmitting and receiving. The short dashed lines in Figures 14(a), 14(b), and 14(c) represent the results when $J_o$ Bessel shading is used in transmitting while Gaussian shading with its $f$-num-

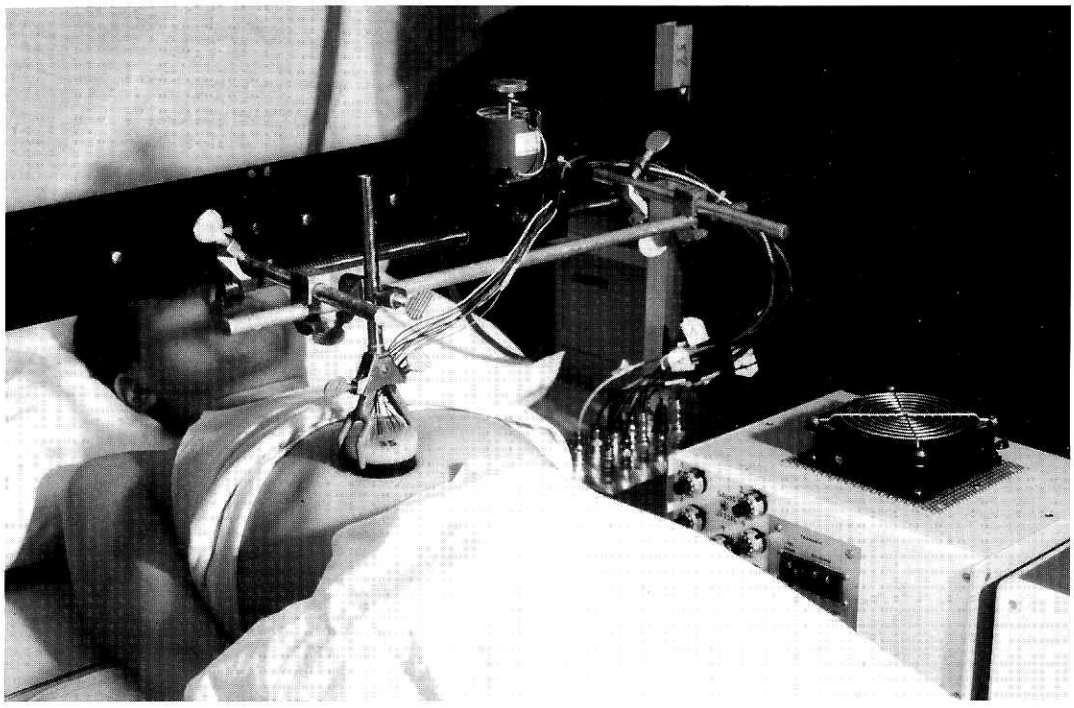

(a)

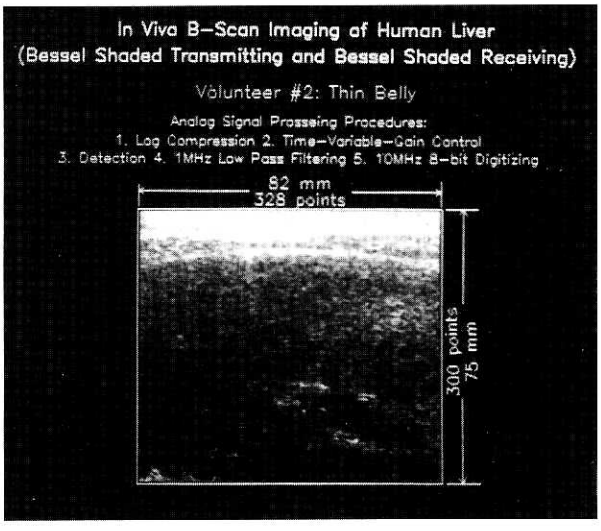


(b)

Fig. 13. Photograph of the *in vivo* experimental system. (b) *In vivo* pulse-echo imaging of the human liver. The size of the image is 82 mm × 75 mm. The left side of the image corresponds to the center of the belly, while the right-hand side corresponds to the side of the body. Scanning direction was from left to right.

ber equal to $Z/D$ is used in receiving. The long dashed lines in Figs. 14(a), 14(b) (combined into solid line), and 14(c) show the response when transmitting with a single-focus Gaussian beam ($f$-number is fixed to 2.4), while receiving with Gaussian shading with an $f$-number always equal to $Z/D$. This simulates the case that the dynamic focusing pulse-echo imaging system is set to single transmitting mode, which has the same imaging frame rate as that when transmitting with $J_o$ Bessel beam. Figure 14(d) shows the responses when the transducer is shaded by $J_o$ Bessel function in both transmitting and receiving at differ-

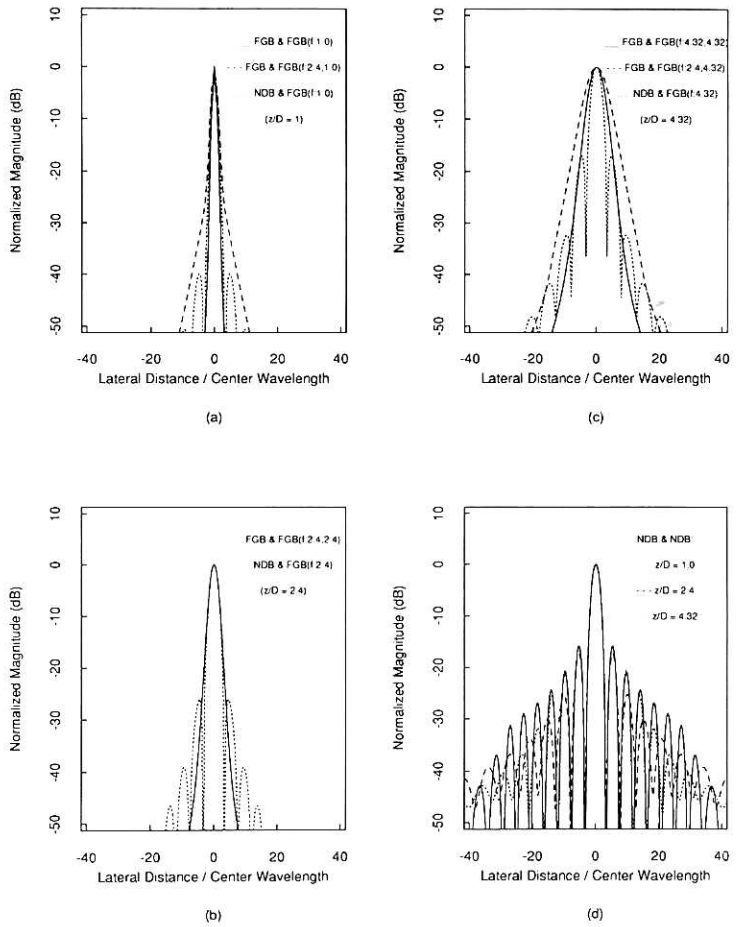


Fig. 14. Simulations of sidelobe and beam width of the pulse-echo imaging systems with various combinations of transmitting/receiving shading at $Z/D$ (distance/diameter) = (a) 1.0, (b) 2.4, and (c) 4.32, respectively. In (a), (b), and (c) solid lines, short dashed lines, and long dashed lines correspond to the combinations of both transmitting and receiving with dynamically focused Gaussian beams, transmitting with $J_o$ Bessel nondiffracting beam while receiving with dynamically focused Gaussian beam and transmitting with a single focus Gaussian beam ($f$-number = 2.4) while receiving with dynamically focused Gaussian beam, respectively. (d) $J_o$ Bessel nondiffracting shading is used in both transmitting and receiving at $Z/D$ = 1.0, 2.4, and 4.32, respectively. Center wavelength of the pulse is 0.6 mm and the diameter of the transducer is 50 mm. The character $f$ in each figure represents the $f$-number of the focused Gaussian beam.

ent distances, $Z/D$ = 1.0 (solid line), 2.4 (long dashed line), and 4.32 (short dashed line). The geometry and the parameters of the transducer in Fig. 2 were used in the simulations. The system transfer functions of the transducer and electrical excitation pulse were assumed to be the same as those in the previous simulations in the third section.

From Fig. 14, it is seen that the dynamically focused receiving suppresses the sidelobes of the $J_o$ Bessel beam dramatically at all distances in the depth of field [compare Fig. 14(d) to short dashed lines in Figs. 14(a), 14(b), and 14(c)]. The imaging system with the nondiffracting beam/dynamic focusing combination has lower sidelobes as well as higher resolution (small main beam width) than the system with single-focus transmitting/dynamic receiving away from the transmitting focus [see Figs. 14(a) and 14(c)], and is comparable to the system with dynamic focusing in both transmitting and receiving [compare short dotted lines with solid lines in Figs. 14(a), 14(b), and 14(c)]. Therefore, when dynamic focusing in receive is combined with the nondiffracting beam in transmit, high-resolution, and high-contrast images can be expected at high-frame rates.

## *Conclusion*

The advantages and disadvantages of the Bessel beam and the conventional focused Gaussian beam

Table 2. List of advantages and disadvantages of the Bessel beam and the conventional focused Gaussian beam for pulse-echo imaging and tissue characterization.

| Conclusion | $J_o$ Bessel nondiffracting beam | Conventional focused Gaussian beam |
|---|---|---|
| Advantages | 1. Large depth of field which eliminates multiple focusing in transmitting<br>2. Easier beam correction in tissue characterization when Bessel shading is used in both transmitting and receiving | 1. Low sidelobes which will generate high-contrast imaging in depth of field<br>2. In focus field intensity and receiving sensitivity are increased greatly [see Figs. 4(a), 4(b)], which increases the signal-to-noise ratio around the focus (in near field only) |
| Disadvantages | 1. Larger sidelobes (determined by Bessel function)<br>2. High-peak intensity is required to obtain high signal-to-noise ratio | 1. Short depth of field<br>2. Complex beam correcting procedures for tissue characterization |

for pulse-echo imaging and tissue characterization are listed in Table 2.

Images having good resolution and contrast can be obtained by transmitting a $J_o$ Bessel nondiffracting beam and using conventional dynamically focused receiving.

*Acknowledgments*—This work was supported in part by grant CA-43920 from the National Institutes of Health. The authors appreciated the help of Randall R. Kinnick for building the pulse-echo circuits of the nondiffracting transducer and for setting up the scanning mechanics for *in vivo* human experiment. The authors also appreciated the help given by Dr. Robert C. Bahn and Mr. Gerald E. McGrath in the Department of Pathology for making the sliced human liver sample. The authors also thank Dr. E. Meredith James and Duane M. Brakke of the Department of Radiology for providing the ACUSON 128 commercial B-scanner and Mr. David J. Anders and Mr. Darrel T. Rowe of the Department of Imaging Maintenance for providing the RMI413A tissue equivalent phantom. The authors are grateful for the secretarial assistance of Elaine C. Quarve and graphic assistance of Christine A. Welch.

## REFERENCES

Alasaarela, E.; Koivukangas, J. Evaluation of image quality of ultrasound scanners in medical diagnostics. J. Ultrasound Med. 9:23–34; 1990.

Durnin, J. Exact solutions for nondiffracting beams. I. The scalar theory. J. Opt. Soc. Am. 4(4):651–654; 1987.

Hsu, D. K.; Margetan, F. J.; Thompson, D. O. Bessel beam ultrasonic transducer: Fabrication method and experimental results. Appl. Physics Letter 55(20):2066–2068; 1989.

Hsu, D. K.; Margetan, F. J.; Hasselbush, M. D.; Wormley, S. J.; Hughes, M. S.; Thompson, D. O. Technique for nonuniform poling of piezoelectric element and fabrication of Gaussian transducers. IEEE Trans. UFFC 37(5):404–410; 1990.

Lu, J.-Y.; Greenleaf, J. F. Ultrasonic nondiffracting transducer for medical imaging. IEEE Trans. UFFC 37(5):438–447; 1990

Ziolkowski, R. W.; Lewis, D. K.; Cook, B. D. Evidence of localized wave transmission. Phys. Rev. Lett. UME 62(2):147–150; 1989.